A&A 673, A97 (2023)
https://doi.org/10.1051/0004-6361/202245513

Astronomy & Astrophysics

LBT-MODS spectroscopy of high-redshift candidates in the *Chandra* J1030 field

A newly discovered $z \sim 2.8$ large-scale structure

Stefano Marchesi[1,2,3], Marco Mignoli[1], Roberto Gilli[1], Giovanni Mazzolari[3,1], Matilde Signorini[4,5], Marisa Brienza[1,3], Susanna Bisogni[6], Micol Bolzonella[1], Olga Cucciati[1], Quirino D'Amato[7], Alessandro Peca[8], Isabella Prandoni[9], Paolo Tozzi[5], Cristian Vignali[3,1], Fabio Vito[1], and Andrea Comastri[1]

[1] INAF – Osservatorio di Astrofisica e Scienza dello Spazio di Bologna, Via Piero Gobetti, 93/3, 40129 Bologna, Italy
e-mail: stefano.marchesi@inaf.it
[2] Department of Physics and Astronomy, Clemson University, Kinard Laboratory of Physics, 140 Delta Epsilon Ct., Clemson, SC 29634, USA
[3] Dipartimento di Fisica e Astronomia, Università degli Studi di Bologna, via Gobetti 93/2, 40129 Bologna, Italy
[4] Dipartimento di Fisica e Astronomia, Università degli Studi di Firenze, via G. Sansone 1, 50019 Sesto Fiorentino, Firenze, Italy
[5] Istituto Nazionale di Astrofisica (INAF) – Osservatorio Astrofisico di Arcetri, Largo E. Fermi, 50125 Firenze, Italy
[6] INAF – Istituto di Astrofisica Spaziale e Fisica Cosmica Milano, Via A. Corti 12, 20133 Milano, Italy
[7] Scuola Internazionale Superiore di Studi Avanzati (SISSA), Via Bonomea 265, 34136 Trieste, Italy
[8] Department of Physics, University of Miami, 1320 S Dixie Highway, Coral Gables, FL 33146, USA
[9] INAF – Istituto di Radioastronomia, via P. Gobetti 101, 40129 Bologna, Italy

Received 20 November 2022 / Accepted 21 March 2023

ABSTRACT

We present the results of a spectroscopic campaign with the Multi-Object Double Spectrograph (MODS) instrument mounted on the Large Binocular Telescope (LBT), aimed at obtaining a spectroscopic redshift for seven *Chandra* J1030 sources with a photometric redshift ≥2.7 and optical magnitude $r_{\rm AB}$ = [24.5−26.5]. We obtained a spectroscopic redshift for five out of seven targets: all of them have $z_{\rm spec} \geq 2.5$, thus probing the reliability of the *Chandra* J1030 photometric redshifts. The spectroscopic campaign led to the serendipitous discovery of a $z \sim 2.78$ large-scale structure (LSS) in the J1030 field: the structure contains four X-ray sources (three of which were targeted in the LBT-MODS campaign) and two non-X-ray-detected galaxies for which a VLT-MUSE spectrum was already available. We also find 26 galaxies with a photometric redshift in the range $z_{\rm phot}$ = [2.68−2.88], which we consider candidate LSS members. The X-ray members of the LSS are hosted in galaxies that are significantly more massive ($\log(M_*/M_\odot)$ = [10.0−11.1]) than both those hosting the two MUSE-detected sources ($\log(M_*/M_\odot) < 10$) and those belonging to the photometric sample (median stellar mass $\log(M_*/M_\odot) = 10.0$). Both observations and simulations show that massive galaxies, and particularly objects with $\log(M_*/M_\odot) > 10$, are among the best tracers of LSSs and filaments in the cosmic web. Consequently, our result can explain why X-ray-detected active galactic nuclei have also been shown to be efficient tracers of LSS.

Key words. galaxies: active – galaxies: distances and redshifts – X-rays: galaxies – galaxies: high-redshift

1. Introduction

The formation and evolution of galaxy clusters is a widely debated topic, involving multiple complex processes. These include, for example, merging and interaction of gas-rich galaxies, growth of supermassive black holes (SMBHs) at galaxy centers, and the consequent active galactic nuclei (AGN) feedback (either positive or negative) on the intra-cluster medium and on the star formation (SF) processes (e.g., Overzier 2016). In gas-rich, overdense regions, evolutionary processes likely take place faster and/or more efficiently than in field galaxies, as shown through measurements of the mass-metallicity relation at $z \sim 0$ (e.g., Peng & Maiolino 2014). Furthermore, several works have shown that at $z > 2$, the X-ray AGN activity is enhanced in sources in protoclusters with respect to those in the field (e.g., Pentericci et al. 2002; Digby-North et al. 2010; Lehmer et al. 2013; Martini et al. 2013; Vito et al. 2020; Tozzi et al. 2022), and a similar trend is also observed in terms of SF activity (e.g., Capak et al. 2011; Umehata et al. 2015, 2019; Gilli et al. 2019; Kubo et al. 2019; Chapman et al. 2023). The study of large-scale structures (LSSs) at $z > 2$ hence represents an ideal way to investigate all of these processes, and understand the evolving path that leads to $z \sim 0$ galaxy clusters.

Cosmological simulations show that only a minor part of the whole structure mass lies within the inner part of a protocluster, in the so-called main halo, which is the most massive among the many progenitor halos that will eventually merge in the $z \sim 0$ cluster (see, e.g., Muldrew et al. 2015). Indeed, at $z \sim 2$, about 80% of the protocluster mass and member galaxies are expected – on average – to reside outside the main halo, over a scale of several megaparsec. Muldrew et al. (2015) also show that this behavior is mass–dependent, meaning that the progenitors of more massive clusters extend over larger scales. For this reason, a full understanding of the physics and evolution of a LSS requires tracking sources over an area of several square megaparsec (i.e., at $z \sim 2$–3, over field of views of at least ∼15′×15′; see also Chiang et al. 2013). To this end, faint X-ray-selected AGN have been shown to be excellent

tracers of LSSs (see, e.g., Gilli et al. 2003; Silverman et al. 2010; Marchesi et al. 2021). For example, Gilli et al. (2003) identified several spikes in the redshift distribution of X-ray sources in the *Chandra* Deep Field-South, with some of which containing three to four X-ray sources only. All of these LSSs were eventually confirmed with extended photometric and spectroscopic campaigns (Castellano et al. 2007; Salimbeni et al. 2009; Balestra et al. 2010).

Recently, *Chandra* targeted – with a deep, ∼0.5 Ms observation – a 335 arcmin^2 region centered on the $z = 6.31$ quasar (QSO) SDSS J1030+0525. SDSS J1030+0525 is one of the first QSOs detected at $z > 6$ by the Sloan Digital Sky Survey (SDSS; Fan et al. 2001). This field is known to be highly biased since it hosts both a galaxy overdensity at $z = 6.3$, around SDSS J1030+0525 (Morselli et al. 2014; Balmaverde et al. 2017; Mignoli et al. 2020), and another overdensity at $z = 1.7$, around a Fanaroff-Riley type II (FRII) radio galaxy (Nanni et al. 2018; Gilli et al. 2019; D'Amato et al. 2020). The flux limit achieved by the *Chandra* J1030 survey (Nanni et al. 2020) makes this the fifth deepest X-ray field to date: the survey contains 256 sources detected down to a 0.5–2 keV flux limit of $f_{0.5-2\,\mathrm{keV}} = 6{\times}10^{-17}$ erg s^{-1} cm^{-2}. Such a deep flux limit makes J1030 an ideal region to search for intrinsically faint and/or heavily obscured AGN. Optical/near-infrared (NIR) counterparts selected in r, z, J, and 4.5 µm were associated with the X-ray sources using standard likelihood-ratio matching techniques. Spectroscopic and photometric redshifts have been computed in Marchesi et al. (2021, hereafter M21) for 243 extragalactic sources out of the 256 *Chandra* J1030 ones[1]. As reported in M21, X-ray sources appear to efficiently trace LSSs in the *Chandra* J1030 field too. In fact, multiple significant X-ray structures are detected in the field in the redshift range $z = [0.15-1.5]$, all of which were confirmed (mostly with increased significance) when extending the analysis to non-X-ray sources.

The spectroscopic completeness of deep X-ray surveys, while fairly high when considering samples in their entirety (up to ∼50–70%; see, e.g., Luo et al. 2017 on the *Chandra* Deep Field-South 7 Ms survey; Marchesi et al. 2016a on the *Chandra* COSMOS-Legacy survey; M21 on the *Chandra* J1030 survey), is significantly biased against high-redshift sources. In particular, at redshift $z > 3$ (i.e., at epochs before the peak in AGN and SF activity, see, e.g., Madau & Dickinson 2014; Ueda et al. 2014; Buchner et al. 2015; Ananna et al. 2019; Peca et al. 2023) only a few hundred X-ray-selected AGN from X-ray surveys have been spectroscopically confirmed[2]. Such a result is not surprising given that more distant sources are expected to be fainter and therefore more difficult to be identified spectroscopically. In the *Chandra* J1030 survey, while a spectroscopic redshift was measured for 123 out of 256 sources, only three of them have $z_{\mathrm{spec}} > 3$, one of which being the $z = 6.3$ QSO at the center of the J1030 field.

Within this framework, here, we present the results of a spectroscopic campaign with the Multi-Object Double Spectrograph (MODS) mounted on the Large Binocular Telescope (LBT) which targeted *Chandra* J1030 sources with a photometric redshift $z_{\mathrm{phot}} \geq 2.7$. The paper is organized as follows: in Sect. 2 we report on new spectroscopic and photometric observations of the J1030 field we recently performed. In Sect. 3 we then present the results of the LBT-MODS spectroscopic campaign, while in Sect. 4 we use the new spectroscopic redshifts to report on the discovery of a $z \sim 2.8$ LSS in the J1030 field. We finally summarize the results of the paper in Sect. 5. In Appendix A we also present the updated photometric redshifts for the $z > 2$ *Chandra* J1030 sources which we computed using the new LBT Large Binocular Camera (LBC)'s g band and the Wide-field InfraRed Camera (WIRCAM)-CFHT's Ks band photometry, and we used the new redshifts to update the *Chandra* J1030 $z > 3$ number counts.

Through the rest of the work, we assume a flat ΛCDM cosmology with $H_0 = 69.6$ km s^{-1} Mpc^{-1}, $\Omega_m = 0.29$, and $\Omega_\Lambda = 0.71$ (Bennett et al. 2014). Errors are quoted at the 90% confidence level, unless otherwise stated.

2. New spectroscopic and photometric coverage of the J1030 field

Among the 26 *Chandra* J1030 sources with photometric redshift $z_{\mathrm{phot}} \geq 2.7$ and no spectroscopic redshift available in the M21 catalog, we selected seven targets that were bright enough ($r_{\mathrm{AB}} \lesssim 26.5$) to obtain an optical spectrum with LBT-MODS. Since we used a multi-object spectrograph such as MODS, we also included 12 more *Chandra* J1030 sources that were randomly located inside the footprint of the two masks and lacked a spectroscopic redshift. These additional targets had photometric redshift in the range $z_{\mathrm{phot}} = [0.9-2.2]$.

Our LBT-MODS observations were performed on January 31 and February 5, 2022: each of the two masks was observed for a total of four hours. Since LBT is made of two telescope units of 8.4m diameter with each being equipped with similar instrumentation (and in particular with the identical MODS1 and MODS2 spectrographs), the total time on target is actually halved. Our MODS spectra have been obtained in dichroic mode using both the blue G400L (3500–5900 Å) and the red G670L (5400–10 000 Å) gratings on the blue and red channels. As shown in the following paragraphs, the wide wavelength range we obtained by using this specific combined configuration (the same adopted in M21) made it possible to detect emission and absorption features over a wide range of wavelengths and to measure a significant number of spectroscopic redshifts reliably. We reduced the data using the Spectroscopic Interactive Pipeline and Graphical Interface (SIPGI) tool that has been specifically developed to reduce optical/NIR data from slit-based spectrographs (Gargiulo et al. 2022).

The data reduction pipeline is organized as follows. We created calibration frames for both MODS1 and MODS2 for each of the two sets of observations (i.e., for each of the two masks). Specifically, a bad pixel map was produced with imaging flats and applied to every observed frame, along with a correction for cosmic rays. Each frame was independently bias subtracted and flat-field corrected through a master flat obtained from a set of spectroscopic flats. The inverse solution of the dispersion, obtained from a set of arc lamps' frames and stored in the master lamp, was applied to individual frames for the wavelength calibration and the removal of any curvature due to optical distortion. The mean accuracy we achieved on the wavelength calibration is 0.09 Å for the red and 0.07 Å for the blue channel. Two-dimensional wavelength-calibrated spectra were then extracted and sky subtracted. The sensitivity function, obtained thanks to the observations of the spectro-photometric standard stars GD153 and GD71, was applied to obtain flux-calibrated

[1] Out of the remaining 13 objects, seven are stars and six lack an optical/NIR counterpart and therefore cannot be classified.

[2] This number does not include those objects, mostly unobscured Type 1 QSOs, which were detected at other wavelengths and then followed up with X-ray facilities (see, e.g., Nanni et al. 2017; Vito et al. 2019).

spectra. Finally, wavelength- and flux-calibrated, sky-subtracted spectra were stacked together and the one-dimensional spectrum of each source was extracted.

The targets' redshifts have been measured on the one-dimensional spectra: for the MODS observations, the wavelength coverage allowed for a Lyα detection down to $z = 1.9$, where the Lyα emission line is often the only detectable feature for our faint objects. All the emission line centers were determined using a Gaussian fit to the line profile: the only exception was the Lyα feature of XID 011 where, due to the structured shape, we adopted the line peak to determine the redshift. For all the solutions for which the single emission line was identified as Lyα, we can confidently rule out other possible redshift solutions. Lower redshift solutions would imply the detection of other nearby lines, as is the case for the X-ray sources with $z < 1.5$ presented in Appendix B. Also, in all the objects belonging to the $z \sim 2.78$ structure, the emission line is asymmetric with a red wing and, when the spectra signal-to-noise allows it, the underlying continuum shows a clear break at the wavelength of the Lyα line. Both spectral characteristics are typical of the high-redshift Lyα line.

Our group was also recently granted time to observe the J1030 field with LBT-LBC in the g band (observations performed in May 2021; total exposure 1800 s; PI M. Mignoli) and with WIRCAM-CFHT in the Ks band (observations performed in February 2022; total exposure 6400 s; PI M. Mignoli). We will present a detailed description of the data analysis process, as well as an updated photometric catalog, in Mignoli et al. (in prep.). Here we briefly summarize the improvement provided by these observations with respect to the photometric catalog we used in M21.

The g band imaging (3σ magnitude limit $g_{\rm AB} = 27.5$) covers a band that was previously missing in our photometric coverage of the field, and its depth almost matches the depth we achieved in the adjacent r band (magnitude limit $r_{\rm AB} = 27.5$). The J1030 field was instead already observed in the Ks band as part of the MUSYC survey. However, our new Ks data is ∼3 magnitudes deeper (3σ magnitude limit $Ks_{\rm AB} = 24$) than the MUSYC K-Wide (Blanc et al. 2008) image we used in M21, and ∼1 magnitude deeper than the MUSYC K-Deep coverage of the central $10'\times10'$ of the J1030 field (Quadri et al. 2007). In Sect. 4, we take advantage of this new photometric information to compute the stellar masses and star formation rates (SFRs) of the galaxies belonging to a newly detected $z \sim 2.78$ LSS in the J1030 field, as well as the photometric redshifts of non-X-ray sources in the J1030 field, searching for more candidate members of the same structure. In Appendix A, we instead show how we used the data from this imaging campaign to refine the *Chandra* J1030 photometric redshifts and to derive the $z > 3$ X-ray number counts in the J1030 field.

3. Results of the LBT-MODS spectroscopic campaign

We report in Table 1 the redshift values we obtained, together with a breakdown of the different features detected in the spectra. We measured a spectroscopic redshift for five out of seven sources in our main sample of high-redshift candidates: all of them have $2.5 < z_{\rm spec} < 3.1$. No clear feature was detected instead in the spectra of XID 378 and XID 381. As reported in Table 1, the photometric redshifts computed in M21[3] efficiently selected high–redshift candidates: all five $z \geq 2.7$ candidates for which we obtained a spectroscopic redshift have $z_{\rm spec} \geq 2.5$. This increases the *Chandra* J1030 spectroscopic completeness at $z > 2.5$ (from eight to 13 out of 40 *Chandra* J1030 sources with $z > 2.5$, i.e., from 20% to 33%) and shows that the *Chandra* J1030 photometric redshifts can reliably select high-redshift candidates. We also measured a spectroscopic redshift for seven out of the 12 *Chandra* J1030 filler sources at $0.9 < z < 2.2$ lacking a spectroscopic redshift.

As reported in Table 1, all the targets for which we computed a spectroscopic redshift in this work (both the primary targets and the fillers) are classified as emission line galaxies (ELGs). In M21, we define ELGs as sources whose spectra do not show any detectable AGN features, but a flat or bluish continuum and low–ionization emission lines that are compatible with a typical SF activity. These sources' optical emission is therefore dominated by non-AGN processes, and we can assess their AGN nature only thanks to the X-ray detection, since their X-ray luminosity $L_{2-10\,\rm keV}$ is way above the $10^{42}\,\rm erg\,s^{-1}$ threshold which is commonly adopted to select AGN in the X-rays. Notably, in M21, the ELG population we sampled had a much lower average redshift ($\langle z_{\rm ELG,M21}\rangle = 1.08$, with a standard deviation of $\sigma_{\rm z,ELG,M21} = 0.58$) and it was therefore significantly brighter ($\langle r_{\rm AB,ELG,M21}\rangle = 23.0$, with a standard deviation of $\sigma_{\rm r,ELG,M21} = 1.8$; as a reference, the targets analyzed in this work have $\langle r_{\rm AB,ELG}\rangle = 25.3$, with a standard deviation of $\sigma_{\rm r,ELG} = 1.0$). In two targets (XID 102, $z = 1.1084$; XID 206, $z = 1.124$; see Figs. B.1 and B.2) we find tentative evidence of the [NeV] narrow emission line, which is a known tracer of obscured AGN (see, e.g., Maiolino et al. 1998; Vignali et al. 2006, 2010; Mignoli et al. 2013; Cleri et al. 2022; Barchiesi et al. 2023).

From Table 1, as well as from Fig. 1, where we report the *Chandra* J1030 sources' total AB magnitudes (from Nanni et al. 2020) as a function of spectroscopic redshift, it can also be understood how this spectroscopic campaign significantly increased the spectroscopic completeness of the faint ($r_{\rm AB} \geq 24$) *Chandra* J1030 population, from 28 to 40 sources. It is worth noting that this new campaign, targeting fainter sources than in M21, led to the detection of no new broad line AGN (BL-AGN). In the M21 sample, 43 out of 123 sources with a spectroscopic redshift (35%) were BL-AGN; as it can be seen in Fig. 1, BL-AGN are more easily detected at brighter magnitudes, so that 21 out of 50 sources with $r_{\rm AB} \leq 23$ are BL-AGN (42%); whereas, out of 31 sources in M21 with $z_{\rm spec}$ and $r_{\rm AB} \geq 24$, only eight (26%) were BL-AGN. Following the spectroscopic campaign reported in this work, the BL-AGN fraction at magnitudes $r_{\rm AB} \geq 24$ decreased to 19%.

In M21, we also extensively discuss how the lack of narrow-band photometry in the J1030 field makes BL-AGN the class of targets for which the photometric redshifts are significantly less accurate: in more detail, only 28 out of 43 BL-AGN (i.e., 65%) had a photometric redshift in agreement with the spectroscopic one (where the agreement is achieved when $\|z_{\rm phot} - z_{\rm spec}\|/(1 + z_{\rm spec}) < 0.15$). As a reference, 25 out of 28 ELGs (i.e., 89%) had photometric redshifts in agreement with the spectroscopic ones. Consequently, the fact that we did not find any new BL-AGN in the *Chandra* J1030 optically faint subsample has also the indirect result of strengthening the reliability of the photometric redshifts for the 108 targets lacking a $z_{\rm spec}$. In fact, the vast majority of them (87 out of 108, 81%) have $r_{\rm AB} \geq 24$.

Finally, two of the targets in the sample (XID 008, $z_{\rm spec} = 2.78$; XID 011, $z_{\rm spec} = 2.767$) were also part of the sample studied in Peca et al. (2021). That work analyzes a subsample of 54 *Chandra* J1030 sources with a hardness ratio (HR; i.e., the ratio

[3] All high-z candidates but XID 381 have been observed in at least 11 photometric bands. XID 381 has been observed in nine bands.

Table 1. Summary of the redshift measurements obtained in the LBT-MODS campaign presented in this work.

ObjID	RA hh:mm:ss	Dec dd:mm:ss	r_{AB}	z_{spec}	Q_z	Class	$z_{phot,M21}$	$z_{phot,new}$	Spectral features (obs λ)
XID 007	10:30:29.77	+05:22:32.26	25.21	2.7799	2	ELG	$3.24^{+1.30}_{-1.30}$	$3.22^{+1.28}_{-1.28}$	Lyα (4595 Å)
XID 008	10:30:28.10	+05:22:58.75	24.41	2.7797	2	ELG	$3.34^{+0.90}_{-0.90}$	$2.68^{+1.02}_{-1.02}$	Lyα (4597 Å), NV
XID 011	10:30:27.89	+05:23:13.42	26.67	2.7674	2	ELG	$4.34^{+2.10}_{-2.10}$	$4.16^{+1.48}_{-1.48}$	Lyα (4581 Å)
XID 151	10:30:41.54	+05:26:25.13	25.25	3.041	2	ELG	$2.74^{+0.88}_{-0.88}$	$2.96^{+0.52}_{-0.52}$	Lyα (4912 Å)
XID 158	10:30:28.01	+05:28:08.35	24.83	2.505	1	ELG	$3.37^{+1.19}_{-1.17}$	$2.12^{+0.88}_{-0.88}$	Lyα (4262 Å), NV
XID 378	10:30:38.13	+05:24:03.31	26.5	–	0	None	$5.45^{+1.03}_{-1.05}$	$1.92^{+2.82}_{-0.04}$	None
XID 381	10:30:43.12	+05:25:26.99	25.06	–	0	None	$3.44^{+1.56}_{-1.56}$	$3.86^{+1.00}_{-1.00}$	None
XID 029	10:30:38.00	+05:26:13.09	26.66	–	0	None	$2.22^{+0.80}_{-0.80}$	$2.15^{+2.11}_{-0.77}$	None
XID 066	10:30:32.31	+05:28:07.35	23.99	2.1113	2	ELG	$2.15^{+0.40}_{-0.39}$	$1.84^{+0.34}_{-0.34}$	Lyα (3783 Å), NV
XID 098	10:30:31.05	+05:27:47.32	27.3	–	0	None	$1.49^{+0.59}_{-0.57}$	$5.21^{+0.91}_{-0.89}$	None
XID 102	10:30:31.61	+05:29:04.44	25.6	1.1084	2	ELG	$5.44^{+0.46}_{-0.46}$	$1.72^{+1.78}_{-1.40}$	MgII, [OII], [NeV]
XID 103	10:30:29.79	+05:29:09.09	24.65	1.4990	1	ELG	$1.44^{+0.20}_{-0.20}$	$1.50^{+0.22}_{-0.22}$	[OII]
XID 153	10:30:28.29	+05:27:40.72	27.02	–	0	None	$2.16^{+3.26}_{-0.26}$	$4.44^{+1.74}_{-1.74}$	None
XID 198	10:30:39.95	+05:26:55.23	24.1	–	0	None	$1.35^{+0.15}_{-0.17}$	$1.02^{+0.26}_{-0.22}$	None
XID 206	10:30:14.76	+05:29:19.80	>27.5	1.124	1	ELG	$1.48^{+3.44}_{-1.00}$	$1.48^{+3.44}_{-1.00}$	[OII], [NeV]
XID 214	10:30:44.59	+05:25:44.77	25.97	–	0	None	$1.38^{+0.54}_{-0.01}$	$1.44^{+0.92}_{-0.01}$	None
XID 365	10:30:27.88	+05:23:48.31	25.72	1.4159	1	ELG	$1.83^{+0.39}_{-0.37}$	$1.73^{+0.29}_{-0.31}$	[OII], [OIII]
XID 366	10:30:28.58	+05:32:24.61	24.52	1.0474	2	ELG	$0.92^{+0.22}_{-0.22}$	$0.84^{+0.20}_{-0.20}$	[OII], [NeIII]
XID 369	10:30:31.28	+05:28:02.30	24.7	0.8248	2	ELG	$1.17^{+0.05}_{-0.07}$	$1.17^{+0.05}_{-0.03}$	[OII], [OIII], Hγ, Hβ

Notes. The identification number is taken from the *Chandra* J1030 catalog (Nanni et al. 2020). Furthermore, r_{AB} is the AUTO magnitude in the r band, as reported in Nanni et al. (2020); z_{spec} is the source spectroscopic redshift; Q_z is the quality flag for z_{spec} (2: secure; 1: uncertain; 0: no measurement); "Class" is the spectral classification (ELG: emission line galaxy; None; no classification); and $z_{phot,M21}$ is the photometric redshift computed in Marchesi et al. (2021) and used to select the high-redshift candidates, while $z_{phot,new}$ is the updated photometric redshift computed using the new g- and Ks-band photometric information presented in Sect. 2, as described in Appendix A.

between the difference between 2–7 keV and 0.5–2 keV source counts, and 0.5–7 keV source counts) of HR> −0.1 and at least 50 net counts in the 0.5–7 keV band. Since low-energy, soft photons are more easily absorbed by the obscuring material surrounding accreting SMBHs, sources with larger HR values are more likely to be obscured. In such targets, features such as the fluorescent Iron Kα line at 6.4 keV and the 7.1 keV Iron edge are particularly prominent and can be used to determine the source redshift through X-ray spectral fitting (see, e.g., Maccacaro et al. 2004; Civano et al. 2005; Vignali et al. 2015; Simmonds et al. 2018; Marchesi et al. 2019; Iwasawa et al. 2020). The X-ray spectrum of each of the 54 targets was then fit leaving the redshift free to vary, and thus using the X-ray features mentioned above to determine the targets redshifts.

Peca et al. (2021) measured an X-ray redshift of $z_X = 2.80^{+0.05}_{-0.05}$ for XID 008, where the Iron Kα line was detected. Such a measurement is in excellent agreement with the spectroscopic redshift, particularly considering the uncertainties as to the measurement, which are much smaller than the photometric redshift ones. The method was instead less effective in XID 011, where the X-ray redshift measurement ($z_X = 1.94^{+1.05}_{-0.38}$) was based on the tentative detection of the Iron edge. Even in this second target, however, the X-ray redshift is consistent with the spectroscopic one within the errors.

4. A new structure at $z \sim 2.8$

As mentioned in the Introduction, faint X-ray-selected AGN have been shown to be excellent tracers of LSSs, and in M21 we report several J1030 structures detected in the *Chandra* J1030 up to redshift $z \sim 1.5$. Thanks to the LBT-MODS spectroscopic campaign presented in this work, we are now able to identify a new LSS in the J1030 field, with this one located at a significantly larger redshift, $z \sim 2.78$. We report in Table 2 the overdensity members and their properties, while in Fig. 2 we plot the redshift cumulative distribution function around $z \sim 2.78$ of both the *Chandra* J1030 sources and of all the sources in J1030 with a spectroscopic redshift. As we have already discussed in M21, such a representation provides a good visualization of candidate redshift structures in the field, which readily appear as sharp cumulative distribution function rises, and it is free of binning issues. Four sources in the overdensity are X-ray detected, namely XID 007, XID 008, XID 011, and XID 109. For this work, we measured a spectroscopic redshift for XID 007, XID 008, and XID 011, while the redshift of XID 109 ($z = 2.771$) has already been reported in M21 and was also obtained using the MODS spectrograph. From this same plot, it can be noticed that two other potential overdensities are observed at $z \sim 2.37$ and $z \sim 2.51$. While the signal-to-noise ratios (S/Ns) of these two groups of sources are lower than the one we adopt to select an overdensity, $S/N = 3.8$, we plan to further investigate these candidate structures in a follow-up work.

In addition to the four X-ray $z \sim 2.78$ sources, there are two more J1030 objects that are not X-ray detected and have $z_{spec} \sim 2.78$: for both targets, we measured the redshift using the Multi Unit Spectroscopic Explorer (MUSE) instrument mounted on the European Southern Observatory (ESO) Very Large Telescope (VLT). A $\sim 1' \times 1'$ region of the J1030 field centered on

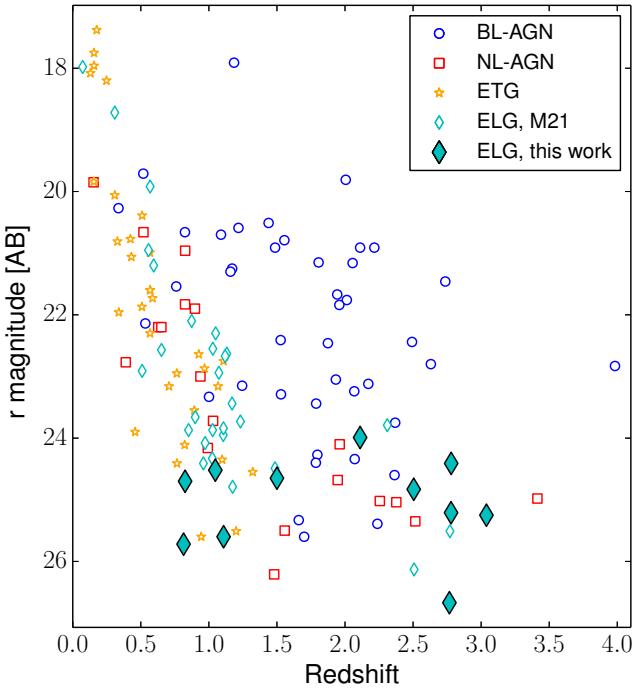

Fig. 1. Total AB magnitude in the r band from Nanni et al. (2020) as a function of spectroscopic redshift for the 122 *Chandra* J1030 sources with $z_{\rm spec}$ from M21 (open markers): we do not include in this plot the $z = 6.3$ QSO SDSSJ1030+0525, which is not detected in the r band. BL-AGN are plotted as blue circles, narrow-line AGN as red squares, emission line galaxies as cyan diamonds, and early-type galaxies as orange stars. The emission line galaxies reported in this work are plotted as full cyan diamonds.

the $z = 6.3$ QSO was observed by MUSE (Bacon et al. 2010, 2015) between June and July 2016 under the program ID 095.A-0714 for a total of ~6.4 hours of exposure time. The data reduction of the MUSE observations is presented in Gilli et al. (2019). The final data cube has a wavelength range of 4750–9350 Å, a spectral sampling of 1.25 Å, and a spatial sampling of 0.2″, covering an area of 1 sq-arcmin centered at the sky position of the QSO SDSSJ1030+0524. The one-dimensional spectra were extracted by combining the spaxels inside a three-pixel aperture that matches the seeing full width at half maximum of 0.6″. The MUSE wavelength coverage did not allow for the Lyα region at $z \sim 2.78$ to be accessed, but the high S/N spectra of the two galaxy members present a rich plethora of spectral features, both in emission (HeII 1640 Å and CIII] 1909 Å lines) and in absorption – interstellar medium (ISM) lines – that provided accurate redshift measurements via cross-correlation with a high-z star-forming template (Talia et al. 2012).

We report the flux–calibrated, one-dimensional spectra of the six members of the LSS in Fig. 3. The spectra of the remaining targets for which we measured a redshift are reported in Appendix B.

For consistency with the approach we used in M21, we used the method presented in Gilli et al. (2003), and earlier in Cohen et al. (1999), to compute the significance of the structure. Sources were first distributed in velocity space $V = c\ln(1+z)$ rather than in redshift space since dV corresponds to local velocity variations relative to the Hubble expansion. The velocity distribution was then smoothed twice: once with a broad Gaussian, with $\sigma_B = 1.5{\times}10^4$ km s^{-1} to create the expected background distribution of the sample; and the second one with a narrower Gaussian with $\sigma_S = 300$ km s^{-1}, which is the typical velocity dispersion observed in galaxy structures (e.g., Cohen et al. 1999; Gilli et al. 2003). We then computed $S/N = (S - B)/\sqrt{B}$, where S is the number of sources within $\Delta V = \pm 800$ km s^{-1} around the peak $z = 2.775$ ($S = 4$ in the X-ray-detected sample, $S = 6$ in the whole one), and B is the number of background sources in the same interval; ΔV was chosen to optimize the S/N value. We obtained a $S/N = 6.3$ for the X-ray overdensity and $S/N = 5.5$ when the non-X-ray-detected J1030 sources were included in the computation. The Poisson probability of observing S sources given the estimated background value B is $P_{\rm Poiss(N\geq N_{obj,X})} = 3{\times}10^{-4}$ for the X-ray LSS, while we obtained $P_{\rm Poiss(N\geq N_{obj,All})} = 5{\times}10^{-5}$ for the whole LSS. We note that this is among the highest redshift X-ray LSSs ever detected: for example, in the CDF-S 7 Ms (Luo et al. 2017), the two farthest X-ray-detected LSSs are at $z \sim 2.57$ and $z \sim 3.47$. The SSA22 *Chandra* survey (Lehmer et al. 2009; Radzom et al. 2022) instead found 13 X-ray members of the SSA22 protocluster at $z = 3.09$, which was, however, first detected through a optical spectroscopy follow-up of candidate $z \sim 3$ Lyman break galaxies (Steidel et al. 1998). We note that the main difference between high-z LSSs detected in the optical with respect to those detected in the X-rays is the type of sources used to trace the LSS: in optical surveys the most common tracers are Lyman break galaxies (see, e.g., Toshikawa et al. 2016) and Lyα and Hα emitters (e.g., Higuchi et al. 2019; Koyama & Polletta 2021), while in the X-rays the tracers are AGN. Thus, by detecting and studying X-ray LSSs, one can simultaneously study the properties of the host and those of the accreting SMBH, and compare the properties of the AGN with those of AGN at similar redshifts that are not located in overdensities.

We also computed the distance between the different structure members, assuming a flat ΛCDM cosmology (see Introduction). At the average redshift of the targets in the structure, $z = 2.775$, the angular-to-physical conversion factor is 8.026 kpc/″. Five out of six targets (namely, XID007, XID008, XID011, and the two MUSE-detected galaxies) are separated by distances in the range $d_{\rm A} = 100$–1360 kpc (see Fig. 4, right panel). The closest pairs of objects are the two MUSE–detected targets ($d_{\rm A} = 101$ kpc) and XID008 and XID011 ($d_{\rm A} = 120$ kpc). As shown in Fig. 4 (left panel), XID109 is located farther away from the rest of the objects, at ~3.3–4.6 Mpc. The difference in redshift between the targets can also be converted in angular diameter distances: for the sources in the LSS, it varies in the range 30 kpc (XID 007 and XID 008; $\Delta z = 2{\times}10^{-4}$) to 2 Mpc (XID008 and XID011, $\Delta z = 1.25{\times}10^{-2}$). We note that a separation of several megaparsec between AGN belonging to the same structure was also previously reported in Shen et al. (2021), where three AGN were found to be part of a protocluster at $z \sim 3.3$. Two of these AGN lied within ~1 Mpc, while the third one was found at ~5 Mpc from the remaining two.

4.1. Candidate overdensity members based on their photometric redshift

By combining the new g- and K_s-band imaging data presented in Sect. 2 with the existing multiband photometry, we computed photometric redshifts for all the K_s−selected sources in the J1030 field (Mignoli et al. in prep.). We report in Table 3 the optical/NIR photometric bands we used to compute these photometric redshifts. Following the same approach we used in M21, the spectral energy distributions (SEDs) of the sources were fitted using two different codes: `Hyperz` (Bolzonella et al. 2000) and `EAzY` (Brammer et al. 2008). We adopted the

Table 2. Properties of the members of the $z \sim 2.78$ large-scale structure detected in this work.

ObjID	RA hh:mm:ss	Dec dd:mm:ss	z	N_H 10^{22} cm^{-2}	$\log(L_{2-10\,keV})$ erg s^{-1}	$\log(M_*/M_\odot)$	SFR_{SED} $M_\odot$ yr^{-1}	$SFR_{1.4GHz}$ $M_\odot$ yr^{-1}	$\log(L_{1.4\,GHz})$ W Hz^{-1}
XID 007	10:30:29.8	+05:22:32.3	2.7799	<3.9	$44.08^{+0.08}_{-0.08}$	10.49±0.24	165±107	103±35	$23.52^{+0.13}_{-0.18}$
XID 008	10:30:28.1	+05:22:58.8	2.7797	$47.0^{+23.1}_{-21.7}$	$44.46^{+0.11}_{-0.12}$	10.36±0.29	<188	<96	<23.47
XID 011	10:30:27.9	+05:23:13.4	2.7674	$39.4^{+20.0}_{-18.6}$	$44.90^{+0.11}_{-0.12}$	10.24±0.71	82±74	<91	<23.58
XID 109	10:30:41.7	+05:16:12.5	2.771	$2.0^{+8.3}_{-2.0}$	$44.48^{+0.11}_{-0.10}$	11.10±0.13	234±188	197±61	$23.89^{+0.12}_{-0.16}$
MUSE 1	10:30:26.4	+05:25:14.5	2.7722	N/A	<43.15	9.49±0.48	85±81	<165	<23.58
MUSE 2	10:30:26.8	+05:25:03.7	2.7791	N/A	<43.15	9.11±0.69	<87	<226	<23.66
Photometric candidates	–	–	2.78±0.10	N/A	N/A	9.97 (0.43)	38.3 (60.9)	–	–

Notes. We note that z is the source redshift; and N_H and $L_{2-10\,keV}$ are the source column density and intrinsic, 2–10 keV luminosity as computed from the X-ray spectrum (Signorini et al. 2023). Since the two MUSE targets are not detected in the X-rays, their N_H cannot be computed: the $L_{2-10\,keV}$ upper limit was computed from the *Chandra* J1030 survey flux limit in the 2–10 keV band ($f_{2-10\,keV,lim} = 2.7\times10^{-16}$ erg s^{-1} cm^{-2}). Also, M_* is the stellar mass content of the host galaxy (in units of solar masses) and SFR_{SED} is the host star formation rate: both of these quantities were computed through spectral energy distribution fitting. We also report, for comparison, the median and standard deviation of the stellar mass and star formation rates of the 26 galaxies in the J1030 field whose photometric redshift is consistent with $z = 2.78$ (see the text for more details). Finally, $SFR_{1.4\,GHz}$ is the SFR independently derived from the 1.4 GHz luminosity $L_{1.4GHz}$ measured from the JVLA J1030 survey (D'Amato et al. 2022). The $SFR_{1.4GHz}$ values reported here were obtained assuming a Chabrier initial mass function. Upper limits are reported at the 3σ confidence level.

Calzetti et al. (2000) extinction law to take reddening into account, and we used 75 templates dominated by stellar emission, following the work by Ilbert et al. (2013). In more detail, 19 out of 75 are empirical templates from the SWIRE template library (Polletta et al. 2007): seven for elliptical galaxies, 12 for different classes of spiral galaxies (S0, Sa, Sb, Sc, Sd, and Sdm). The other 12 templates describe the SED of starburst galaxies, although no emission lines are included in the template. Finally, the remaining 44 templates are based on the Bruzual & Charlot (2003) stellar population synthesis models, and have been first introduced in Ilbert et al. (2009, 2013).

We used photometric redshifts to identify potential members of the $z = 2.78$ overdensity. To do so, we conservatively selected only those sources that have a photometric redshift in the range $z_{phot} = [2.68-2.88]$ according to both `Hyperz` and `EAzY`. We chose such a range because the RMS of the difference between spectroscopic and photometric redshifts in the J1030 sample at $z > 2$ is $\Delta z \sim 0.1$. Overall, our sample of $z \sim 2.78$ photometric candidates contains 26 galaxies. We report in Fig. 4 the distribution of the sources over the J1030 field.

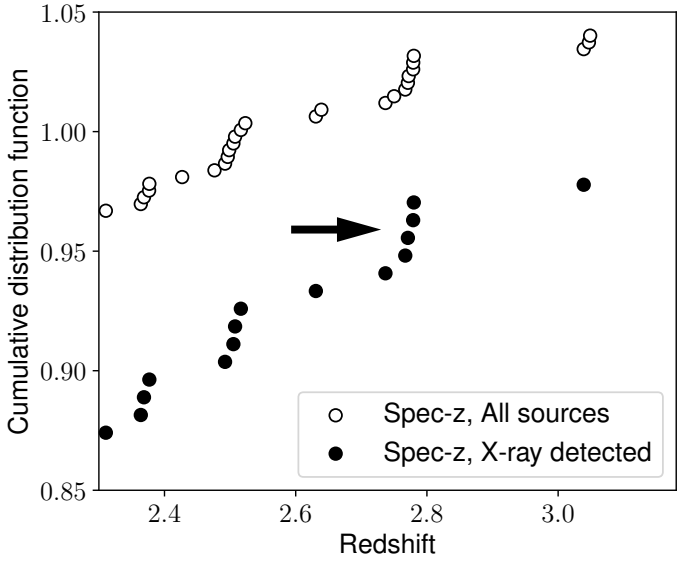

Fig. 2. Redshift cumulative distribution function around $z = 2.78$ for the *Chandra* J1030 sources with a spectroscopic redshift (full markers), and for all the J1030 sources with a spectroscopic redshift, including the non-X-ray-detected ones (empty markers). The overall cumulative distribution function has been shifted by 0.1 for visualization purposes. The $z \sim 2.78$ structure is marked with an arrow. Other two potential structures can be observed at $z \sim 2.37$ and $z \sim 2.51$ (see the text for more details).

4.2. Host properties of the overdensity members

To better understand the properties of the members of the $z \sim 2.78$ overdensity, we took advantage of the excellent multiwavelength coverage of the J1030 field to perform a self-consistent SED fitting from the X-rays to the NIR. To do so, we used the CIGALE v2022.1 tool (Yang et al. 2020, 2022). CIGALE v2022.1 fits a source SED and computes the host galaxy physical properties. With respect to the CIGALE tool (Burgarella et al. 2005; Boquien et al. 2019), CIGALE v2022.1 allows one to also fit the X-ray information, if available. This update to the original tool is particularly helpful to put stronger constraints on the AGN contribution to the SED and, consequently, to obtain more accurate measurements of the host properties.

For the X-ray-detected sources and photometric redshift candidates, we used the optical/NIR photometric information reported in Table 3. For the four X-ray-detected AGN, we also used the 0.5–2 keV and 2–7 keV fluxes reported in Nanni et al. (2020). Finally, both MUSE targets were detected in our new K-band image of the J1030 field. We therefore performed aperture photometry at the K_S position of the sources in the *griz* LBT/LBC bands, as well as in the WIRCAM/CFHT Y and J ones. The two MUSE targets were also detected in the MUSYC BVR catalog, and the MUSE 1 source was also detected in the K-Deep catalog. We therefore included in our SEDs the MUSYC U and V magnitudes from the BVR catalog and the MUSYC H magnitude from the K Deep one. We note that there is an excellent agreement ($\Delta mag \leq 0.05$) between our B and K magnitudes and the MUSYC B_{BVR} and K_{Kd}, a result that supports our choice of using the additional MUSYC data points as we did for the X-ray sources. We also searched the NASA/IPAC Infrared

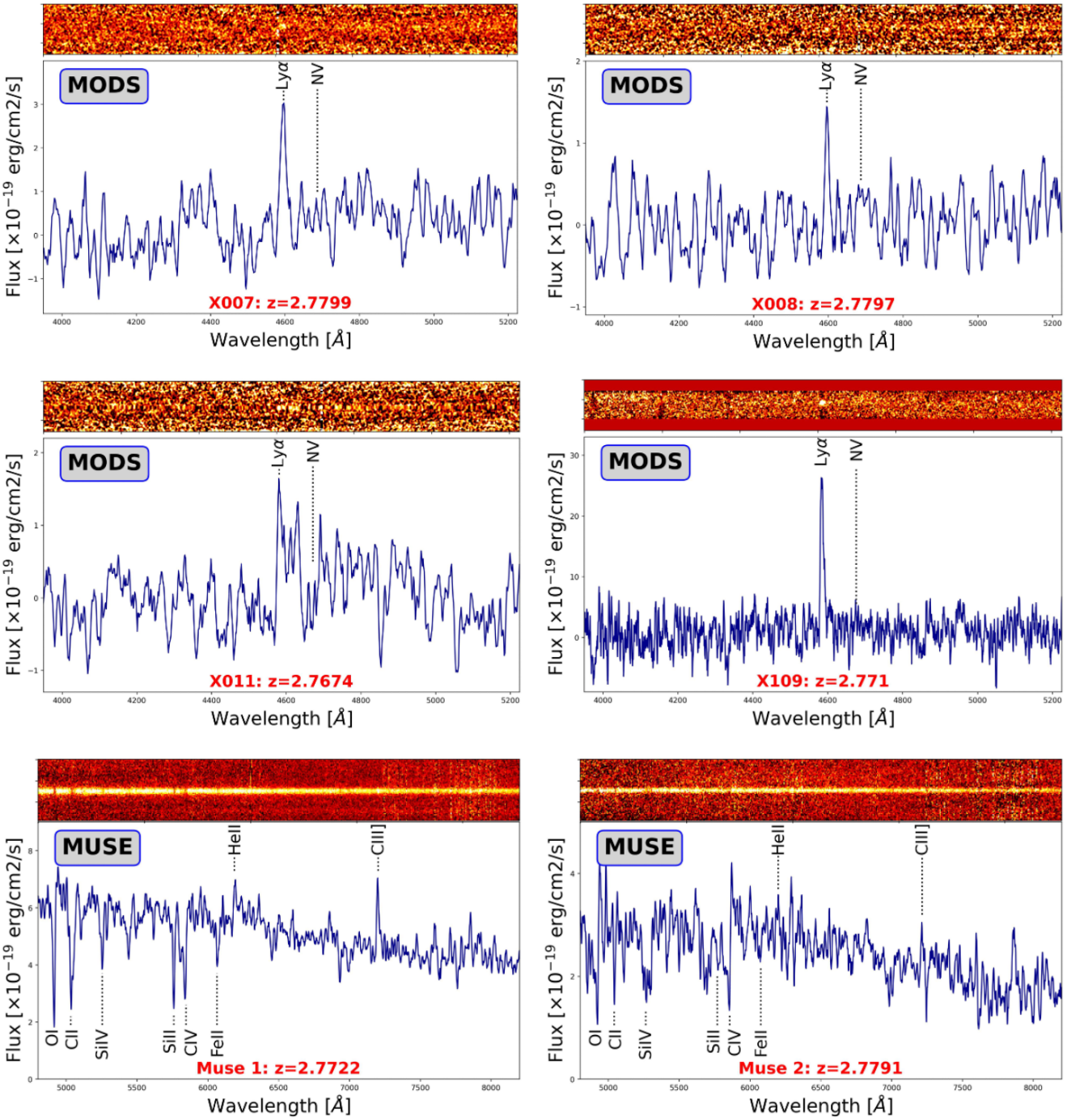

Fig. 3. Flux-calibrated spectra of the six members of the $z \sim 2.78$ LSS: in the top and central panels, we report the LBT-MODS spectra of the four *Chandra* sources; whereas, in the bottom panels, we show the VLT-MUSE spectra of the two sources that are not detected in the X-rays. The spectrum of XID 109 was obtained in the previous *Chandra* J1030 spectroscopic campaign, which we present in Marchesi et al. (2021). We highlighted the expected positions of the main emission lines that fall in the observed spectral range. On top of each one-dimensional spectrum, we report the two-dimensional one.

Science Archive[4] for a WISE counterpart of the two MUSE targets, but we did not find any.

In Table 2 we report the stellar mass M_* and SFR of the six $z \sim 2.78$ LSS members, as well as the median and standard deviation of both parameters for the sample of 26 galaxies with a photometric redshift consistent with $z = 2.78$. As it can be seen, the four X-ray-detected targets are significantly more massive than the two MUSE-detected ones: the stellar mass of the X-ray targets varies in the range $\log(M_*/M_\odot) = [10.2-11.1]$, while the two non-X-ray-detected objects both have $\log(M_*/M_\odot) < 10$. The sample of candidate overdensity members with a photometric redshift of $z_{\rm phot} = [2.68-2.88]$ are also, on average, less massive than the X-ray-detected sources. More specifically, the photometric sample has a median stellar mass of $\log(M_*/M_\odot) = 9.97$ (with a standard deviation of $\sigma = 0.43$); thus, all X-ray sources have stellar masses above the median mass of the photometric

[4] https://irsa.ipac.caltech.edu/

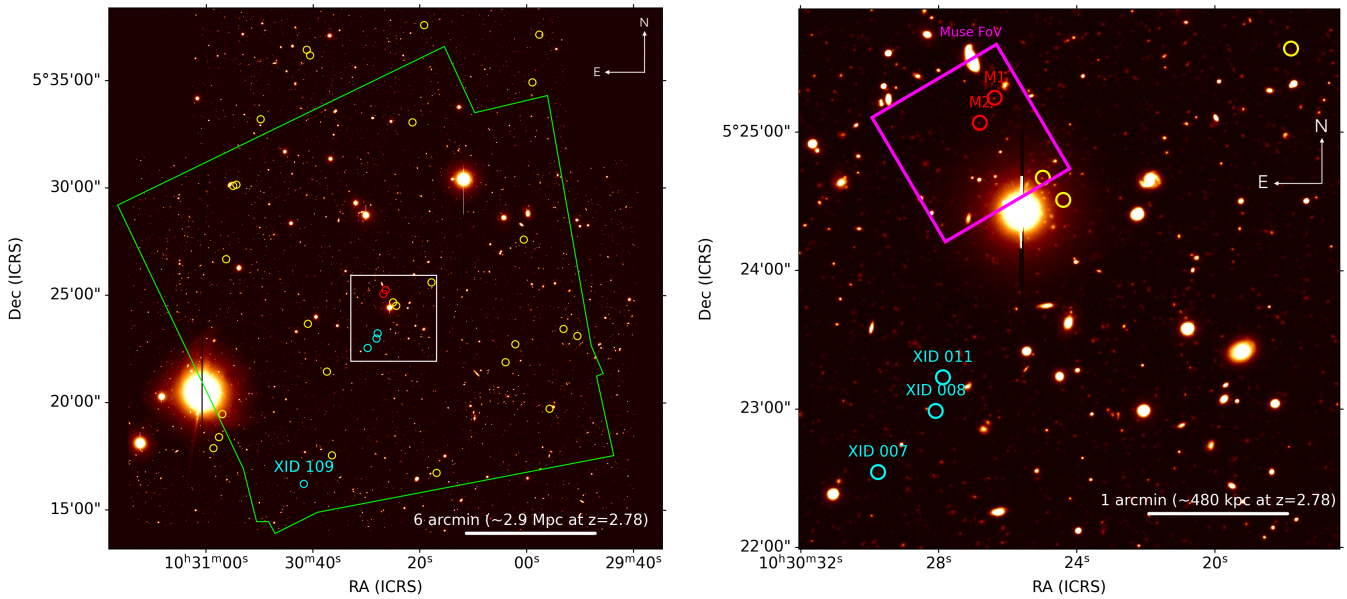

Fig. 4. LBT-LBC r-band images of the J1030 field. Left: whole field image, with the *Chandra* coverage shown in green. The spectroscopically confirmed, X-ray-detected members of the $z \sim 2.78$ LSS are plotted with a red circle, while the two non-X-ray-detected sources with a MUSE spectroscopic redshift are plotted in red. Non-X-ray sources with a photometric redshift in the range $z_{\rm phot} = [2.68-2.88]$ are plotted as yellow circles. Right: Inset of the ~4′×4′ region (shown as a white box in the left panel) where we detected five out of six members of the LSS. The MUSE coverage of the J1030 field is also shown here for reference.

Table 3. Properties of the photometric catalogs used in this work.

Catalog	Filters	Area	5σ Depth $m_{\rm AB}$	Reference
MUSYC BVR	UBV	30′×30′	26.0, 26.2, 26.0	Gawiser et al. (2006)
LBT-LBC	g	23′×25′	26.4	This work.
LBT-LBC	riz	23′×25′	26.8, 26.1, 25.6	Morselli et al. (2014)
HST-ACS	$F775W$	3.3′×3.3′	27.5	Stiavelli et al. (2005)
HST-ACS	$F850LP$	3.3′×3.3′	27.5	Kim et al. (2009)
WIRCAM-CFHT	YJ	24′×24′	24.7, 24.4	Balmaverde et al. (2017)
HST-WFC3	$F160W$	2′×2′	27.5	D'Amato et al. (2020)
MUSYC K Deep	H	10′×10′	23.6	Quadri et al. (2007)
WIRCAM-CFHT	K_s	24′×24′	23.4	This work.
Spitzer-IRAC	CH1-2	35′×35′	22.7, 22.4	Annunziatella et al. (2018)
Spitzer-IRAC	CH3-4	22′×15′	22.1, 21.8	IRSA Archive

population. We also note that our photometric galaxies' sample was K selected, and $K-$selected samples are biased in favor of more massive hosts (see, e.g., Dunne et al. 2009). This further strengthens the significance of detecting X-ray sources in more massive hosts.

As it can be seen in Fig. 3, the two MUSE targets are brighter (in the B band which broadly matches the wavelength range shown in the spectra) than the X-ray targets. More specifically, the two MUSE targets have $B_{\rm AB} \sim 25$, while the X-ray targets all have $B_{\rm AB} > 26$, and actually all but one even have $B_{\rm AB} > 27$. Things change, however, when moving to redder wavelengths. In particular, the X-ray targets are significantly brighter in the K band ($K_{\rm AB} = [22.2-22.7]$) than the MUSE ones ($K_{\rm AB} = [23.4-24.8]$). Such a different behavior at different wavelengths is directly linked to the different host masses observed in the two subsamples: the MUSE targets are likely young, compact sources with intense SF processes ongoing, while the X-ray AGN are hosted in older (thus redder), more massive galaxies.

Massive galaxies, and in particular those sources with $\log(M_*/M_\odot) > 10$, have been shown to be among the best tracers of LSSs and more specifically of filaments in the cosmic web (see, e.g., Malavasi et al. 2017; Sarron et al. 2019; Kuchner et al. 2020). In our case, such a tentative piece of evidence clearly needs to be validated with a larger, statistically more reliable sample. Nonetheless, the significant mass difference between the X-ray and the non-X-ray-detected host galaxies supports a scenario where the X-ray AGN (i.e., those sources with an X-ray luminosity of $L_{2-10\,\rm keV} > 10^{42}\,\rm erg\,s^{-1}$) are hosted by the most massive galaxies in a structure and are therefore more likely to be powered by more massive and more efficient accreting SMBHs. If such a result is to be confirmed in larger samples, it would (at least partially) explain why X-ray-detected targets are such efficient tracers of LSSs.

Quantitatively, using the Suh et al. (2020) $M_{\rm BH}$–M_* relation, we find that the X-ray-detected targets have black hole masses in the range $M_{\rm BH} = [6{\times}10^6\ M_\odot – 7{\times}10^7\ M_\odot]$. Since the Suh et al. (2020) relation was calibrated using X-ray-emitting sources and galaxies with $\log(M_*/M_\odot) > 10$, it cannot be reliably used to estimate the black hole mass of the two MUSE-detected sources. Interestingly, the most massive object among the members of the structure is XID 109, the only one that is not in spatial proximity with the others. Since more massive galaxies are expected to be located at the center of the LSS (this is, for example, the case for the protocluster detected at redshift $z \sim 1.7$ in the J1030 field; see Gilli et al. 2019; D'Amato et al. 2020), such a result could hint at the fact that the center of the structure does not coincide with the region where we detected five out of six LSS members. Indeed, as shown in Fig. 4 (left panel), no clear evidence of clustering is observed when including the photometric redshift candidates in the overdensity. However, any further consideration can be validated only by a spectroscopic follow-up campaign of these candidates.

In Fig. 5, we plotted the SFR as a function of the stellar mass for the six spectroscopically confirmed targets in the LSS, as well as for the 26 photometric candidates. As a reference, we also plotted the Schreiber et al. (2015) M_*-SFR main sequence (MS) at $z \sim 2.95$. As it can be seen, the X-ray-detected sources tend to lie on the MS. One of the two MUSE targets instead has a nominal SFR value well above the MS one for a galaxy with a stellar mass of $\log(M_*/M_\odot) \sim 9.5$; however, the uncertainties as to the SFR for this target are large, and our measurement is consistent with the MS one within the 90% confidence uncertainty. Finally, the majority of photometric candidates also tend to lie on the MS. A few high-mass sources, however, have a SFR much lower than the expected one, thus suggesting that they could already be in a passive, non-star-forming phase. This tentative trend, if spectroscopically confirmed, could then suggest that the X-ray sources in the LSS are hosted not only by the most massive galaxies, but also by objects that are still gas-rich and star-forming.

In Table 2 we also report, for the four *Chandra*–detected targets, the source column density as computed via X-ray spectral fitting (Signorini et al. 2023). Several observational works have shown evidence of an increasing fraction of obscured AGN (i.e., sources with a column density of $N_{\rm H} > 10^{22}\,{\rm cm}^{-2}$ moving from the Local Universe to redshift $z \sim 2$–3 (e.g., La Franca et al. 2005; Tozzi et al. 2006; Liu et al. 2017; Lanzuisi et al. 2018; Vito et al. 2018; Iwasawa et al. 2020; Peca et al. 2023), where sources with $N_{\rm H} > 10^{23}\,{\rm cm}^{-2}$ can reach 70–80% of the overall AGN population. In such a scenario, nuclear obscuration from the so-called obscuring torus, which accounts for almost the totality of obscuration at $z \sim 0$, must be complemented at higher redshifts by nonnuclear absorption taking place within the host galaxy. In particular, a recent work by Gilli et al. (2022) shows that the increasing density with redshift of the ISM can by itself explain the obscured fractions observed at $z \sim 2$–3.

To test this scenario, we worked under the assumption that galaxies where the ISM is denser are also those where the SFR is larger. We report in Table 2 the SFR measurements obtained through SED fitting for the six members of the overdensity. Two out of four X-ray-detected targets (XID 008 and XID 011) have $N_{\rm H} > 10^{23}\,{\rm cm}^{-2}$: in XID 011, we measured significant SF activity ($\rm SFR_{SED} \sim 80\,M_\odot\,yr^{-1}$), while in XID 008 we could only compute a fairly loose upper limit ($\rm SFR_{SED} < 188\,M_\odot\,yr^{-1}$). The two remaining X-ray-detected members of the overdensity (XID 007 and XID 109) both have a column density $N_{\rm H} < 10^{23}\,{\rm cm}^{-2}$: however, for both targets we measured a fairly large SFR, $\rm SFR_{SED} > 100\,M_\odot$. However, the fact that we measured no significant obscuration in the X-ray spectrum of XID 007 and XID 109 could hint at the fact that the source SED is at least partially contaminated by the AGN emission, which would imply that the SFR derived from the SED might be overestimated.

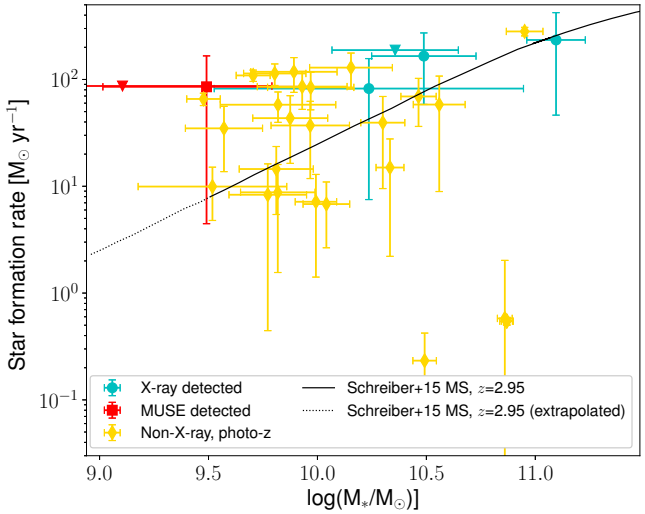

Fig. 5. Star formation rate as a function of stellar mass for the four X-ray detected (cyan circles) and the two MUSE-detected (red squares) members of the $z \sim 2.78$ overdensity, as well as for the 26 candidate members of the overdensity with a photometric redshift of $z_{\rm phot} = [2.68–2.88]$ (yellow diamonds). Upper limits are plotted as downwards triangles. As a reference, we also plotted the $z = 2.95$ main sequence from Schreiber et al. (2015). Both M_* and SFR were computed through SED fitting.

As a consistency check, we therefore independently computed the SFR of the four *Chandra* J1030 sources in the structure by using the radio flux density obtained from a deep JVLA *L*-band observation of the J1030 field (D'Amato et al. 2022). XID 007 and 109 are both detected in the JVLA image, while for the remaining two targets we computed a 3σ upper limit (see Table 2). Since D'Amato et al. (2022) report that their fluxes $S_{1.34\,\rm GHz}$ were measured at 1.34 GHz, we applied a correction factor to compute the 1.4 GHz luminosities reported in Table 2, as follows:

$$L_{1.4\,\rm GHz} = \frac{4\pi D_{\rm L}^2(z)}{(1+z)^{(1+\alpha)}} \left(\frac{1.4\,\rm GHz}{1.34\,\rm GHz}\right)^{\alpha} S_{1.34\,\rm GHz}, \quad (1)$$

where α is the radio photon index and is assumed to be $\alpha = -0.7$ for all targets.

We then used the equation reported in Delvecchio et al. (2021) to derive the SFR:

$$\frac{\rm SFR}{M_\odot\,{\rm yr}^{-1}} = f_{\rm IMF} \times 10^{-24}\, 10^{q_{\rm TIR}(z)}\, \frac{L_{1.4\,\rm GHz}}{\rm W\,Hz^{-1}}, \quad (2)$$

where $L_{1.4\,\rm GHz}$ it the 1.4 GHz luminosity, while $f_{\rm IMF}$ is a correction factor related to the initial mass function (IMF) used in the computation: $f_{\rm IMF} = 1$ for a Chabrier IMF; and $f_{\rm IMF} = 1.7$ for a Salpeter IMF. Finally $q_{\rm TIR}(z)$ is a factor that parameterizes the evolution with both redshift and the host stellar mass of the IR-radio correlation,

$$q_{\rm TIR}(z, M_*) = (2.646 \pm 0.024) \times (1+z)^{-0.023\pm0.008} - (\log M_*/M_\odot - 10) \times (0.148 \pm 0.013). \quad (3)$$

Since the stellar masses and SFRs computed with CIGALE v2022.1 adopted a Chabrier IMF, in Table 2 we report the radio SFR values obtained assuming $f_{\rm IMF} = 1$. As it can be seen, there is a general good agreement between the SED fitting measurements and the 1.4 GHz ones. In particular, for XID 007 and XID 109, we again measured $\rm SFR_{1.4GHz} > 100\,M_{\odot}\,yr^{-1}$. We would like to remind readers, as a caveat, that the Delvecchio et al. (2021) relation was computed using star-forming galaxies, rather than AGN, so the values obtained here are likely upper limits, as part of the radio emission in our targets may be of nuclear origin.

In summary, we do not observe a clear trend between the line-of-sight column density computed through X-ray spectral fitting and the host SFR computed either through SED fitting or through the 1.4 GHz luminosity. Such a result is not in contradiction with the trends discussed in Gilli et al. (2022), since those should be applied statistically on a large sample of sources, and not on single targets. For example, all the known $z \sim 6$ QSOs are by definition unobscured AGN (see, e.g., Nanni et al. 2017; Vito et al. 2019) despite being hosted by young, gas-rich galaxies experiencing significant SF activity.

5. Summary and conclusions

In this work, we have presented the results of a recent LBT-MODS spectroscopic follow-up campaign of a sample of *Chandra*–detected sources in the J1030 field. We also used the LBT-LBC g-band and the CFHT-WIRCAM K_s-band photometry we recently obtained on the J1030 field to update the photometric redshifts of the $z > 2$ candidates in the *Chandra* J1030 sample. The following are the main results of our analysis.

1. Out of seven high-z ($z_{\rm phot} > 2.7$) candidates, we measured a spectroscopic redshift for five sources: all of them have $z_{\rm spec} > 2.5$, thus proving the effectiveness of our photometric redshifts in selecting high-z candidates.
2. All the 12 sources for which we measured a new spectroscopic redshift are classified as ELGs, which means that their optical emission is dominated by non-AGN processes. This result suggests that as we increase the sample spectroscopic completeness at faint magnitudes (all 12 targets have $r_{\rm AB} > 24$), the contribution of the BL-AGN to the overall population significantly decreases.
3. The LBT-MODS spectroscopic campaign led to the serendipitous discovery of a LSS at $z \sim 2.78$ in the J1030 field. The structure contains six spectroscopically confirmed targets, four of which are X-ray detected. Five out of six targets are located within a $\sim 1'$ radius (i.e., within an angular distance $d_{\rm A}$ <1.5 Mpc). Other 26 galaxies have a photometric redshift in the range $z_{\rm phot} = [2.68{-}2.88]$ and are therefore candidate members of the overdensity.
4. We measured a large mass difference between the X-ray-detected AGN and the non-X-ray-detected galaxies in the overdensity: the stellar mass of the X-ray targets varies in the range $\log(M_*/M_{\odot}) = [10.2{-}11.1]$, while the two spectroscopically confirmed, non-X-ray-detected objects both have $\log(M_*/M_{\odot})$<10, and the photometric candidates have median stellar mass $\log(M_*/M_{\odot}) = 10.0$. Massive galaxies are known to be among the best tracers of LSSs: this result, while limited by the small size of the sample, therefore provides a potential explanation of why X-ray-detected AGN also are efficient LSS tracers.
5. We measured in two independent ways – through SED fitting and from the 1.4 GHz luminosity – the SFR of the galaxies hosting the $z \sim 2.78$ overdensity. The two methods give consistent results, and the sources (particularly the X-ray-detected ones) are found to lie on the Schreiber et al. (2015) SFR-M_* MS.
6. With this campaign, we measured a spectroscopic redshift for 12 *Chandra* J1030 sources, thus increasing the sample spectroscopic completeness to 53% (135 out of 256 sources).

Future works will focus on obtaining photometric redshifts for the whole non-X-ray population (Mignoli et al. in prep.) in the J1030 field, and searching for both new members of the LSS and more in general for promising high-z candidates. With a larger number of sources with good photometric redshifts at $z \geq 2$, it will be possible to search for high-redshift overdensities using statistical methods such as the Voronoi tessellation Monte Carlo algorithm (see, e.g., Cucciati et al. 2018; Lemaux et al. 2018, 2022; Shen et al. 2021). These photometric redshifts will also be used to select candidates for new spectroscopic follow-up campaigns with LBT-MODS and other facilities.

Acknowledgements. We thank the referee for the detailed report and the useful suggestion. We acknowledge the support from the LBT-Italian Coordination Facility for the execution of observations, data distribution and reduction. The LBT is an international collaboration among institutions in the United States, Italy and Germany. LBT Corporation partners are the University of Arizona on behalf of the Arizona university system; Istituto Nazionale di Astrofisica, Italy; LBT Beteiligungsgesellschaft, Germany, representing the Max-Planck Society, the Astrophysical Institute Potsdam, and Heidelberg University; The Ohio State University, and The Research Corporation, on behalf of The University of Notre Dame, University of Minnesota and University of Virginia. We acknowledge financial contribution from the agreement ASI-INAF n. 2017-14-H.O. MB acknowledges financial support from the Italian L'Oreal UNESCO "For Women in Science" program and the PRIN MIUR 2017PH3WAT "Blackout".

References

Ananna, T. T., Treister, E., Urry, C. M., et al. 2019, ApJ, 871, 240
Annunziatella, M., Marchesini, D., Stefanon, M., et al. 2018, PASP, 130, 124501
Bacon, R., Accardo, M., Adjali, L., et al. 2010, in Ground-based and Airborne Instrumentation for Astronomy III, eds. I. S. McLean, S. K. Ramsay, & H. Takami, SPIE Conf. Ser., 7735, 773508
Bacon, R., Brinchmann, J., Richard, J., et al. 2015, A&A, 575, A75
Balestra, I., Mainieri, V., Popesso, P., et al. 2010, A&A, 512, A12
Balmaverde, B., Gilli, R., Mignoli, M., et al. 2017, A&A, 606, A23
Barchiesi, L., Vignali, C., Pozzi, F., et al. 2023, A&A, submitted
Bennett, C. L., Larson, D., Weiland, J. L., & Hinshaw, G. 2014, ApJ, 794, 135
Blanc, G. A., Lira, P., Barrientos, L. F., et al. 2008, ApJ, 681, 1099
Bolzonella, M., Miralles, J. M., & Pelló, R. 2000, A&A, 363, 476
Boquien, M., Burgarella, D., Roehlly, Y., et al. 2019, A&A, 622, A103
Brammer, G. B., van Dokkum, P. G., & Coppi, P. 2008, ApJ, 686, 1503
Bruzual, G., & Charlot, S. 2003, MNRAS, 344, 1000
Buchner, J., Georgakakis, A., Nandra, K., et al. 2015, ApJ, 802, 89
Burgarella, D., Buat, V., & Iglesias-Páramo, J. 2005, MNRAS, 360, 1413
Calzetti, D., Armus, L., Bohlin, R. C., et al. 2000, ApJ, 533, 682
Capak, P. L., Riechers, D., Scoville, N. Z., et al. 2011, Nature, 470, 233
Castellano, M., Salimbeni, S., Trevese, D., et al. 2007, ApJ, 671, 1497
Chapman, S. C., Hill, R., Aravena, M., et al. 2023, ApJ, submitted [arXiv:2301.01375]
Chiang, Y.-K., Overzier, R., & Gebhardt, K. 2013, ApJ, 779, 127
Civano, F., Comastri, A., & Brusa, M. 2005, MNRAS, 358, 693
Cleri, N. J., Yang, G., Papovich, C., et al. 2022, ArXiv e-prints [arXiv:2209.06247]
Cohen, J. G., Blandford, R., Hogg, D. W., Pahre, M. A., & Shopbell, P. L. 1999, ApJ, 512, 30
Cucciati, O., Lemaux, B. C., Zamorani, G., et al. 2018, A&A, 619, A49
D'Amato, Q., Gilli, R., Vignali, C., et al. 2020, A&A, 636, A37
D'Amato, Q., Prandoni, I., Gilli, R., et al. 2022, A&A, 668, A133
Delvecchio, I., Daddi, E., Sargent, M. T., et al. 2021, A&A, 647, A123
Digby-North, J. A., Nandra, K., Laird, E. S., et al. 2010, MNRAS, 407, 846
Dunne, L., Ivison, R. J., Maddox, S., et al. 2009, MNRAS, 394, 3
Fan, X., Narayanan, V. K., Lupton, R. H., et al. 2001, AJ, 122, 2833
Gargiulo, A., Fumana, M., Bisogni, S., et al. 2022, MNRAS, 514, 2902
Gawiser, E., van Dokkum, P. G., Herrera, D., et al. 2006, ApJS, 162, 1
Gilli, R., Cimatti, A., Daddi, E., et al. 2003, ApJ, 592, 721
Gilli, R., Comastri, A., & Hasinger, G. 2007, A&A, 463, 79

Gilli, R., Mignoli, M., Peca, A., et al. 2019, A&A, 632, A26
Gilli, R., Norman, C., Calura, F., et al. 2022, A&A, 666, A17
Higuchi, R., Ouchi, M., Ono, Y., et al. 2019, ApJ, 879, 28
Hoaglin, D. C., Mosteller, F., & Tukey, J. W. 1983, Understanding Robust and Exploratory Data Analysis (Wiley)
Ilbert, O., Capak, P., Salvato, M., et al. 2009, ApJ, 690, 1236
Ilbert, O., McCracken, H. J., Le Fèvre, O., et al. 2013, A&A, 556, A55
Iwasawa, K., Comastri, A., Vignali, C., et al. 2020, A&A, 639, A51
Kim, S., Stiavelli, M., Trenti, M., et al. 2009, ApJ, 695, 809
Koyama, Y., Polletta, M., d. C., Tanaka, I., , et al. 2021, MNRAS, 503, L1
Kubo, M., Toshikawa, J., Kashikawa, N., et al. 2019, ApJ, 887, 214
Kuchner, U., Aragón-Salamanca, A., Pearce, F. R., et al. 2020, MNRAS, 494, 5473
La Franca, F., Fiore, F., Comastri, A., et al. 2005, ApJ, 635, 864
Lanzuisi, G., Civano, F., Marchesi, S., et al. 2018, MNRAS, 480, 2578
Lehmer, B. D., Alexander, D. M., Chapman, S. C., et al. 2009, MNRAS, 400, 299
Lehmer, B. D., Lucy, A. B., Alexander, D. M., et al. 2013, ApJ, 765, 87
Lemaux, B. C., Le Fèvre, O., Cucciati, O., et al. 2018, A&A, 615, A77
Lemaux, B. C., Cucciati, O., Le Fèvre, O., et al. 2022, A&A, 662, A33
Liu, T., Tozzi, P., Wang, J.-X., et al. 2017, ApJS, 232, 8
Luo, B., Brandt, W. N., Xue, Y. Q., et al. 2017, ApJS, 228, 2
Maccacaro, T., Braito, V., Della Ceca, R., Severgnini, P., & Caccianiga, A. 2004, ApJ, 617, L33
Madau, P., & Dickinson, M. 2014, ARA&A, 52, 415
Maiolino, R., Salvati, M., Bassani, L., et al. 1998, A&A, 338, 781
Malavasi, N., Arnouts, S., Vibert, D., et al. 2017, MNRAS, 465, 3817
Marchesi, S., Civano, F., Elvis, M., et al. 2016a, ApJ, 817, 34
Marchesi, S., Civano, F., Salvato, M., et al. 2016b, ApJ, 827, 150
Marchesi, S., Ajello, M., Zhao, X., et al. 2019, ApJ, 882, 162
Marchesi, S., Mignoli, M., Gilli, R., et al. 2021, A&A, 656, A117
Martini, P., Miller, E. D., Brodwin, M., et al. 2013, ApJ, 768, 1
Mignoli, M., Vignali, C., Gilli, R., et al. 2013, A&A, 556, A29
Mignoli, M., Gilli, R., Decarli, R., et al. 2020, A&A, 642, L1
Morselli, L., Mignoli, M., Gilli, R., et al. 2014, A&A, 568, A1
Muldrew, S. I., Hatch, N. A., & Cooke, E. A. 2015, MNRAS, 452, 2528
Nanni, R., Vignali, C., Gilli, R., Moretti, A., & Brandt, W. N. 2017, A&A, 603, A128
Nanni, R., Gilli, R., Vignali, C., et al. 2018, A&A, 614, A121
Nanni, R., Gilli, R., Vignali, C., et al. 2020, A&A, 637, A52
Overzier, R. A. 2016, A&A Rev., 24, 14
Peca, A., Vignali, C., Gilli, R., et al. 2021, ApJ, 906, 90
Peca, A., Cappelluti, N., Urry, C. M., et al. 2023, ApJ, 943, 162
Peng, Y.-J., & Maiolino, R. 2014, MNRAS, 438, 262
Pentericci, L., Kurk, J. D., Carilli, C. L., et al. 2002, A&A, 396, 109
Polletta, M., Tajer, M., Maraschi, L., et al. 2007, ApJ, 663, 81
Quadri, R., Marchesini, D., van Dokkum, P., et al. 2007, AJ, 134, 1103
Radzom, B. T., Taylor, A. J., Barger, A. J., & Cowie, L. L. 2022, ApJ, 940, 114
Salimbeni, S., Castellano, M., Pentericci, L., et al. 2009, A&A, 501, 865
Sarron, F., Adami, C., Durret, F., & Laigle, C. 2019, A&A, 632, A49
Schreiber, C., Pannella, M., Elbaz, D., et al. 2015, A&A, 575, A74
Shen, L., Lemaux, B. C., Lubin, L. M., et al. 2021, ApJ, 912, 60
Signorini, M., Marchesi, S., , Gilli, R., et al. 2023, A&A, submitted
Silverman, J. D., Mainieri, V., Salvato, M., et al. 2010, ApJS, 191, 124
Simmonds, C., Buchner, J., Salvato, M., Hsu, L. T., & Bauer, F. E. 2018, A&A, 618, A66
Steidel, C. C., Adelberger, K. L., Dickinson, M., et al. 1998, ApJ, 492, 428
Stiavelli, M., Djorgovski, S. G., Pavlovsky, C., et al. 2005, ApJ, 622, L1
Suh, H., Civano, F., Trakhtenbrot, B., et al. 2020, ApJ, 889, 32
Talia, M., Mignoli, M., Cimatti, A., et al. 2012, A&A, 539, A61
Toshikawa, J., Kashikawa, N., Overzier, R., et al. 2016, ApJ, 826, 114
Tozzi, P., Gilli, R., Mainieri, V., et al. 2006, A&A, 451, 457
Tozzi, P., Pentericci, L., Gilli, R., et al. 2022, A&A, 662, A54
Ueda, Y., Akiyama, M., Hasinger, G., Miyaji, T., & Watson, M. G. 2014, ApJ, 786, 104
Umehata, H., Tamura, Y., Kohno, K., et al. 2015, ApJ, 815, L8
Umehata, H., Fumagalli, M., Smail, I., et al. 2019, Science, 366, 97
Vignali, C., Alexander, D. M., & Comastri, A. 2006, MNRAS, 373, 321
Vignali, C., Alexander, D. M., Gilli, R., & Pozzi, F. 2010, MNRAS, 404, 48
Vignali, C., Iwasawa, K., Comastri, A., et al. 2015, A&A, 583, A141
Vito, F., Gilli, R., Vignali, C., et al. 2014, MNRAS, 445, 3557
Vito, F., Brandt, W. N., Yang, G., et al. 2018, MNRAS, 473, 2378
Vito, F., Brandt, W. N., Bauer, F. E., et al. 2019, A&A, 630, A118
Vito, F., Brandt, W. N., Lehmer, B. D., et al. 2020, A&A, 642, A149
Yang, G., Boquien, M., Buat, V., et al. 2020, MNRAS, 491, 740
Yang, G., Boquien, M., Brandt, W. N., et al. 2022, ApJ, 927, 192

Appendix A: Updated *Chandra* J1030 photometric redshifts and refined high-redshift number counts

As mentioned in Section 2, we recently observed the J1030 field in the g and Ks band. We thus decided to rerun the `Hyperz` tool (Bolzonella et al. 2000) to obtain more reliable photometric redshifts, particularly at z≥2, where a deeper Ks coverage can significantly improve the overall quality of the SED fitting. The new photometric redshifts were computed by using the photometric bands reported in Table 3. We followed the same SED fitting approach we used in M21, to which we refer for a complete description of the different steps. We also generated the redshift probability distribution function (PDZ) of each target.

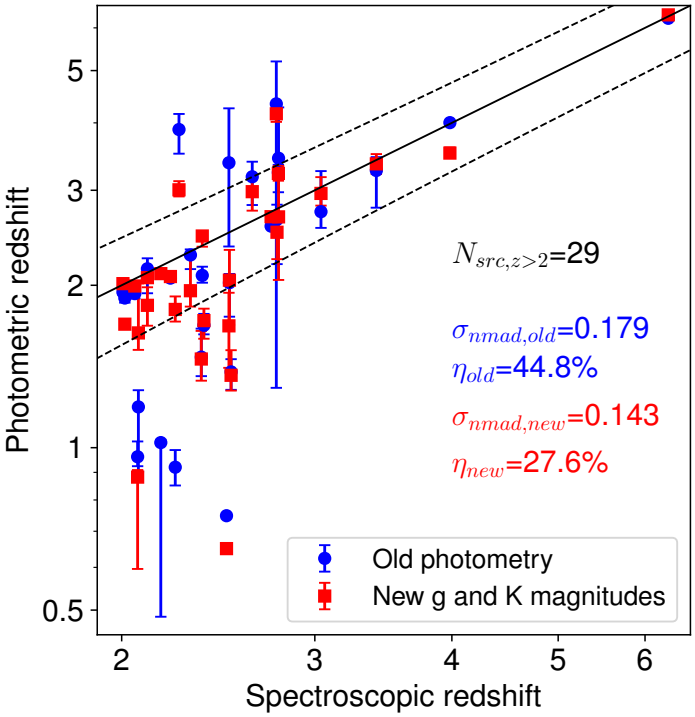

Fig. A.1. Photometric redshift as a function of the spectroscopic one for the 29 J1030 sources with spectroscopic redshift z_{spec} ≥2. The black solid line marks the z_{spec} = z_{phot} relation, while the dashed lines contain the z_{phot} = z_{spec}±0.15(1+z_{spec}) region. Sources within this region are deemed to have a reliable photometric redshift. We note that all the outliers with z_{phot} <1.2 are BL-AGN, a class of sources for which photometric redshifts are generally less reliable (see M21 for more details).

There are 29 *Chandra* J1030 sources with z_{spec} ≥2. We report in Figure A.1 the distribution of the old and new photometric redshifts as a function of the spectroscopic ones. Following the standard approach to estimate a photometric redshift reliability we already used in M21, we assume that z_{spec} and z_{phot} are in agreement when $||z_{phot}-z_{spec}||/(1+z_{spec})<0.15$. The new photometric redshifts are significantly more accurate than the old ones: 21 out of 29 objects (72 %) have $\Delta z/(1+z_{spec})<0.15$, with a normalized median absolute deviation (Hoaglin et al. 1983) $\sigma_{NMAD,new}$ = 1.48 × median[$||z_{phot,new}-z_{spec}||/(1+z_{spec})$] = 0.143. In M21, instead, only 16 out of 29 targets (55 %) showed an agreement between the photometric redshift and the spectroscopic one, with $\sigma_{NMAD,M21}$=0.179. All eight outliers in the new photometric redshift sample are also outliers in the "old" photometric sample; furthermore, two of these outliers (XID011 and XID022) have $z_{phot,new}$ >3. Therefore, while in these two targets the photometric redshifts did not accurately pinpoint the actual source redshift, they were still effective in hinting at a high-redshift solution.

In M21 we computed the z >3 number counts in the *Chandra* J1030 field. We found evidence of a potential overdensity at z >4 with respect to both other X-ray surveys and the predictions of different AGN population synthesis models. However, when we published these results, only three out of 25 z >3 sources had a spectroscopic redshift, one of them (the only one at z_{spec} >4) being the z=6.3 J1030 QSO itself. The z >4 overdensity we measured was therefore based on the photometric redshifts, and in particular on the sources' redshift PDZs.

The spectroscopic campaign we have presented in this work therefore aimed, among other things, to increase the *Chandra* J1030 spectroscopic completeness at z >3, so as to put stronger constraints on the overdensity detection. As reported in Table 1, all the high-z sources that we were able to spectroscopically confirm are in the range z_{spec}=[2.5–3.1]. This, combined with the new photometric redshifts, could in principle affect the *Chandra* J1030 number counts measurements, and in particular reduce the high−z excess presented in M21. For this reason, we recomputed the *Chandra* J1030 z >3 number counts following the same approach presented in M21: most importantly, for sources lacking a spectroscopic redshift and with just a photometric redshift, we did not use the sources nominal best-fit redshift value, but rather their probability distribution functions. As discussed in M21, this is now a common approach when computing the high-z number counts of X-ray surveys, since their spectroscopic completeness strongly decreases at z >2.5–3 (see, e.g., Marchesi et al. 2016b; Vito et al. 2018).

We report in Figure A.2 the *Chandra* J1030 number counts in the redshift bins z=[3–4], z=[4–5], and z=[5–6]: we plotted the original number counts reported in M21 as well as the number counts computed using both the new spectroscopic redshifts and the new photometric redshifts. For comparison, we also report the predictions of the Gilli et al. (2007) AGN population synthesis model and the number counts derived from the Vito et al. (2014) z >3 AGN X-ray luminosity function. As it can be seen, the difference between the number counts computed in M21 and those recomputed in this work using the new spectroscopic and photometric redshifts is marginal, and all number counts are consistent within the uncertainties. In particular, the excess observed at redshift z >4 in M21 is still present, and suggests that one or more additional overdensities can be present in the J1030 field between the z=2.78 and the z=6.3 one. We are now working on the computation of photometric redshifts for all of the sources in the J1030 field (M. Mignoli et al. in prep.) to ultimately use them to search for more high-redshift candidates to then follow-up with spectroscopic campaigns such as the one presented in this paper.

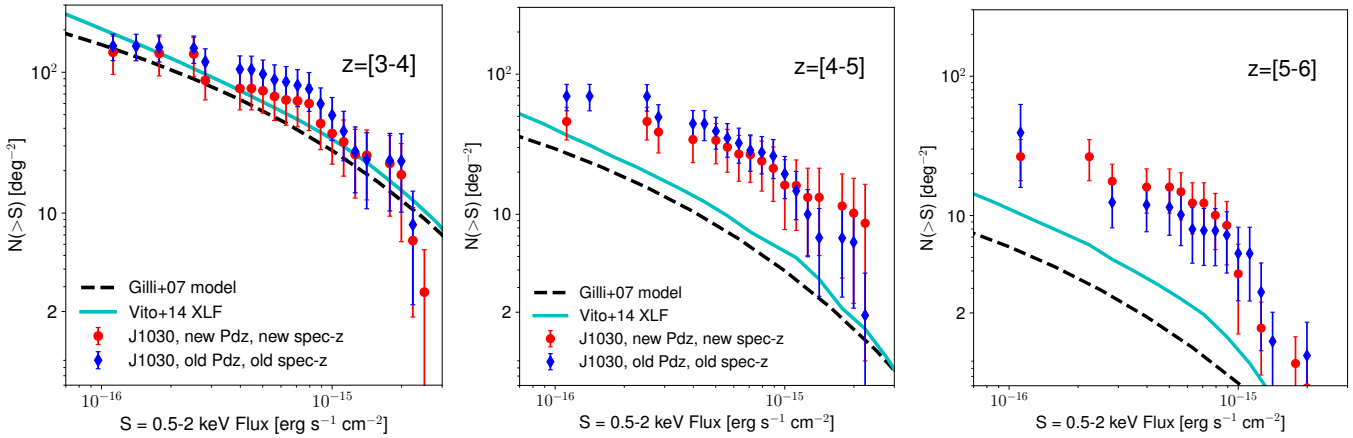

Fig. A.2. *Chandra* J1030 0.5–2 keV number counts in the redshift bins z=[3–4] (left), z=[4–5] (center), and z=[5–6] (right). We plot as red circles the LogN-LogS obtained using both the new spectroscopic redshifts and the new photometric redshifts presented in this work; we instead plotted as blue diamonds the M21 number counts. The number counts in the same redshift ranges derived using the Gilli et al. (2007) AGN population synthesis model (black dashed line) and the Vito et al. (2014) X-ray luminosity function (cyan solid line) are also shown for comparison. The overdensity measured in M21 at z >4 is still present in the newly refined number counts.

Appendix B: Spectra

In Figures B.1 and B.2 in this Appendix, we report the flux-calibrated spectra for the nine sources targeted by our LBT-MODS campaign for which we computed a spectroscopic redshift and that are not part of the z ∼2.78 LSS; the spectra of the LSS are reported in Figure 3. The FITS file of these spectra, as well as of those of the six *Chandra* J1030 for which we could not measure a spectroscopic redshift, are available online[5].

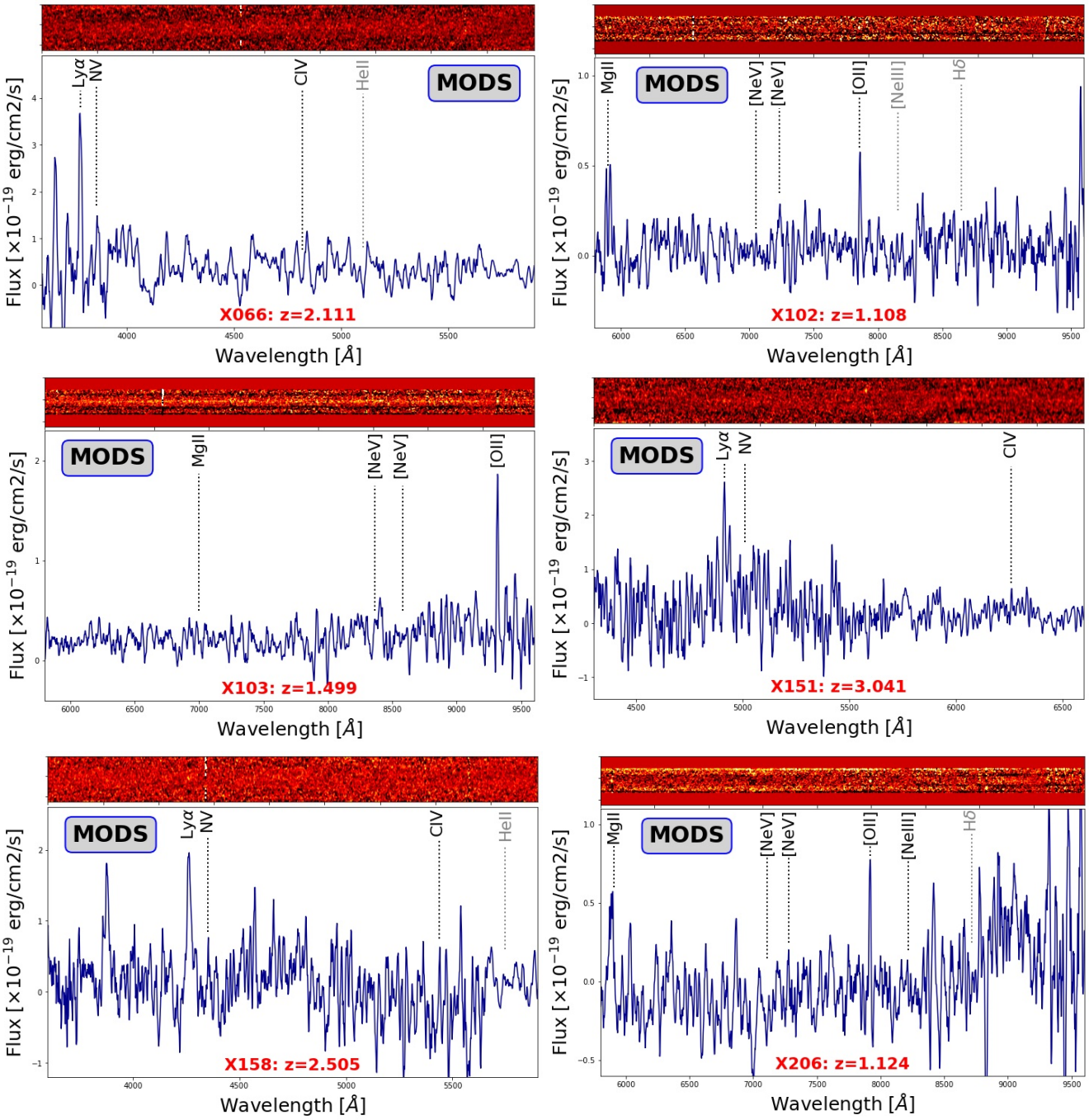

Fig. B.1. LBT-MODS flux-calibrated spectra of six *Chandra* J1030 sources targeted by the campaign presented in this work and not belonging to the z ∼2.78 structure. We highlighted the expected positions of the main emission lines that fall in the observed spectral range. On top of each one-dimensional spectrum, we report the two-dimensional one.

[5] http://j1030-field.oas.inaf.it/~LBTz6/1030/xray_redshift_J1030.html

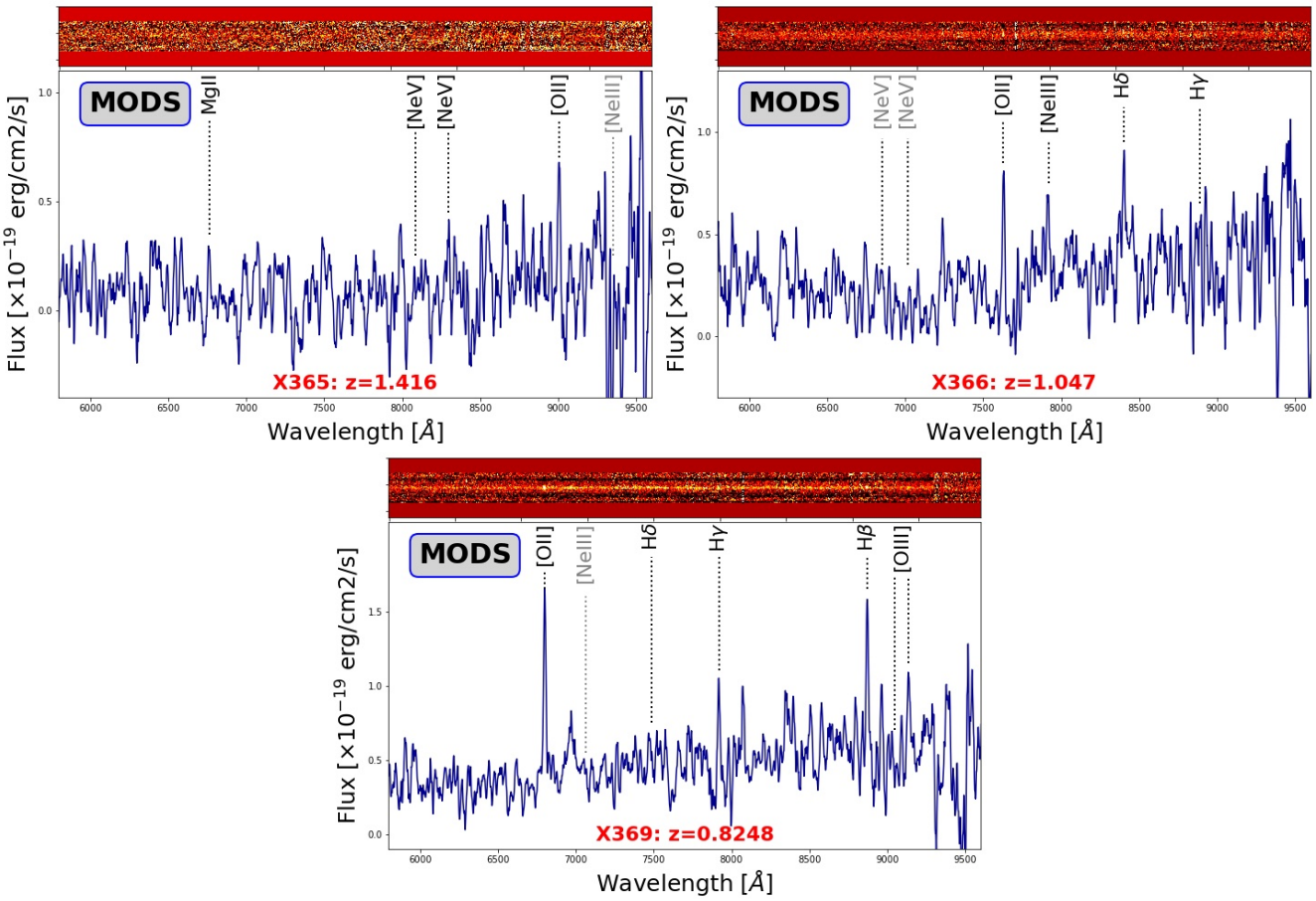

Fig. B.2. LBT-MODS flux-calibrated spectra of three *Chandra* J1030 sources targeted by the campaign presented in this work and not belonging to the z ∼2.78 structure. We highlighted the expected positions of the main emission lines that fall in the observed spectral range. On top of each one-dimensional spectrum, we report the two-dimensional one.